Wave-equation microseismic imaging and event selection in the image domain

Brad Artman[1]*, Ben Witten, Spectraseis Inc.*

Summary

Common techniques for locating fracture events, from large earthquakes to small fractures, are often hampered by the need to pick arrivals in the data domain, which can be onerous or impossible with low signal-to-noise data. Many methods require a significant amount of preprocessing and rigid assumptions about the source location and type. We use the time-reverse imaging algorithm to locate transient microseismic events. The method relies on wave-equation back-propagation of the data, requires no picking or forward modeling, makes no assumptions about the source, and needs minimal preprocessing. We calculate event initiation times and the signal-to-noise ratio in the image domain, then use an intelligent picking algorithm to extract fracture locations. The accuracy is only limited by the correctness of the velocity model. The method, using surface array data, compares well with solutions from down-hole field measurements even with limited velocity information. The method provides a statistical confidence threshold from the data for quality control of the results. These features combine to produce event locations with reduced uncertainty and high precision.

Introduction

Microseismic monitoring has become a common technique to locate fracture events during oil and gas well completion operations. There are numerous techniques including travel-time picking and semblance (Eisner et al., 2008; Maxwell et al., 2010), ray migration methods (Schuster et al., 2004; Borcea et al., 2006; Chambers et al., 2010), and wave-equation based methods (Steiner et al., 2008; Xuan and Sava, 2010). Bardainne et al. (2009) concludes that migration methods using P and S waveforms are superior to picking algorithms.

In this paper, we advocate a (elastic when appropriate) wave-equation method with automatic correlation-based imaging conditions (Artman et al., 2010). Time-reverse imaging (TRI) is accurate, can locate events in low signal-to-noise ratio (S/N) data, requires no picking or forward calculations, and makes no a-priori assumptions about the events. We use a modified version of the TRI algorithm to generate S/N estimates and a statistical confidence threshold in the image domain (Witten and Artman, 2011).

To process very long records with many individual transient events, we generate many S/N sub-images on the fly during continuous back-propagation of the time-reversed data. This maintains the initiation times of events. Focus locations are automatically picked in the image domain with an intelligent algorithm. The algorithm is demonstrated with synthetic surface data and elastic propagation. Acoustic processing with single component data is also possible with the loss of some source mechanism information. A small field example demonstrates the accuracy of the method, compared to down-hole solutions.

Method

This method relies on generating many TRI images (Artman et al., 2010) from consecutive time windows. If one independently images discrete time windows, events that are at the beginning of the time window or span two windows are lost. Instead, we implement continuous propagation of the data, and write out sub-images at regular time intervals. After writing, the working image is zeroed. Thus we ensure all events collapse properly, but avoid the accumulation of stochastic noise energy. We use time windows, length n_t, that are a small multiple of the time it takes for an event to be recorded across the entire array. For n_t of only several wavelengths, sub-images approach the pseudo-Wigner distribution function wave fields proposed in Sava (2011).

Each sub-image is post-processed to calculate an estimate of the image-domain signal-to-noise ratio (I-SNR) (Witten and Artman, 2011). This requires imaging a data-domain noise model as well. Here, we use random data scaled to the RMS values of the traces for each time window. We generate an entire noise-data volume, n, prior to imaging so that 2 parallel continuous imaging processes (data and noise) are launched simultaneously. Each I-SNR image volume is generated by dividing the current data sub-image by the corresponding noise sub-image. This can be done in parallel implementations while the subsequent time window is propagating. The length n_t is further constrained by the need to be long enough to capture meaningful statistics of the stochastic noise such that the confidence threshold calculation for the I-SNR image is robust (Witten and Artman, 2011). Because the time length is regular and the earth-model does not change, a single confidence threshold value is used for all I-SNR sub-images. All model points that fall below the confidence threshold are zeroed or clipped for display.

Therefore, each j^{th} sub-image using the absolute amplitude auto-correlation imaging condition is calculated for every point in space by

$$I_j(\mathbf{x}) = \frac{\sum_{i=(j-1)n_t}^{i+n_t} ||\hat{\mathbf{d}}(\mathbf{x},t_i)||}{\sum_{i=(j-1)n_t}^{i+n_t} ||\hat{\mathbf{n}}(\mathbf{x},t_i)||} \quad , \tag{1}$$

where $\hat{\mathbf{d}}$ and $\hat{\mathbf{n}}$ are the reversed and propagated data and noise-data volumes as function of space and time. Individual images may be saved separately or stacked to produce a single image of multiple events. Zeroing the image amplitudes at locations below the confidence threshold is imperative for stacking since most of the imaging conditions for TRI are not zero mean (Artman et al., 2010). Although stacking minimizes disk requirements, event initiation times are lost and nearby events may blend together. Below, we introduce an automatic picking algorithm to post-process the sub-images such that they need not be saved.

Synthetic Example

For illustration, Figure 1 shows three synthetic microseismic events elastically modeled through the 1D velocity model in Figure 2. The density was a constant 2000 kg/m^3. The model has 2 m resolution in space, a free surface condition at the top and absorbing boundaries along the other sides. The data was recorded at the surface with 65 stations every 25 m, though only every other trace is displayed in the figure.

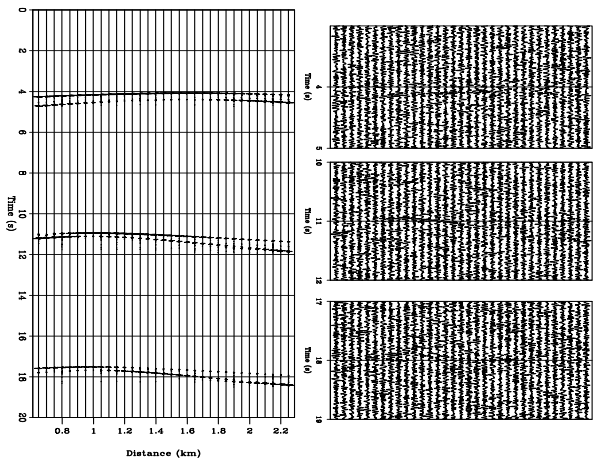

Figure 1 Vertical component of the data. Left: All data, no noise added. Right: Zoom around the three events after adding noise. Time axis of all 4 panels is common.

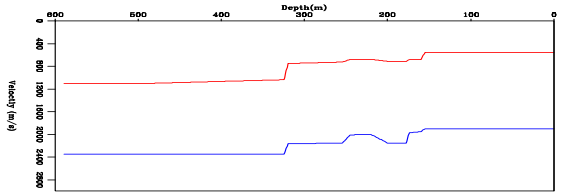

Figure 2 P and S-wave velocity model for forward and reverse propagation.

The 3 events in Figure 1 are randomly oriented single forces generating both P and S waves. The first event is located deep in the section at 900 m. The second and third events are at 400 m depth, and only 30m apart horizontally. Equal energy random noise was added to both components of the data such that the deep event, Figure 1 top-right, has data S/N=0.16. The shallower events have S/N=0.25 and 0.15. The events are very difficult to interpret in the noisy data domain panels. We define $n_t = 2$ s, which is the time for an S wave to propagate across the domain in the surface layer. Choosing 2 s time windows, the first event arrives at the beginning of a time boundary of where different images are written. The third event crosses a time boundary for different images. Without continuous propagation, neither of these events would focus.

Figure 3 displays 4 of the 10 sub-images where amplitudes less than the 99% confidence threshold (I-SNR=1.48 for this model and n_t) are blue. The imaging condition used is the wavefield amplitude auto-correlation, equation 1. The direction of smearing around each event center is a function of the source radiation pattern. Other imaging conditions can be applied to investigate the source more completely (Artman et al., 2010). Only 3 of the sub-images contain focusing above the confidence threshold. Therefore we only include a single all-zero image. With perfect velocity accuracy for the synthetics, the locations of the 3 amplitude maximums have error no greater than 1 grid cell in any direction. Greater errors are expected for less accurate velocity models, although the field data results below using only a 1D profile estimated from a partial open-hole log indicate generally less error than have been reported in the literature (Eisner et al., 2009; Chambers et al., 2009).

The first event in Figure 1 was modelled with excitation time t=3.6 s, and has a minimum travel time to the surface ~ 0.4 s. Therefore, the event arrives across the array between 4 and 4.5 s. When analysing 2 s sub-images, the initiation time parameter of each event is defined at the middle of the time window plus or minus 1 s. The event is focused in the sub-image corresponding to initiation time of 3 ± 1 s, with title 2-4 sec in Figure 3.

The top panel of Figure 4 shows the stack of all 10 sub-images generated from the 20 s of data. The bottom panel is the result of imaging the entire data set, producing a single image. Note the difference of color scales between the images. Overlain on both images are the correct event locations. All 3 events are visible and correctly positioned in the top panel. The 2 shallower events, however, blend together providing an elevated S/N. On the bottom, only event 2 is correctly located. This event has the highest data S/N of the three. However, the energy in the event wavelet is very small compared to the total stochastic noise energy over 20 s. Therefore, the focus has I-SNR=6 in the top panel, and only 1.7 in the lower result. The spurious values on the bottom-right are due to the coherent sum of energy that is below the confidence threshold in the individual sub-images.

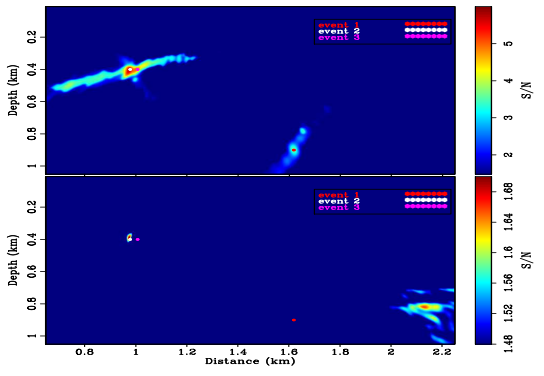

Figure 4 Top: Stack of all 10 two-second images after zeroing. Bottom: Image of the continuous data set. Note the different color scales.

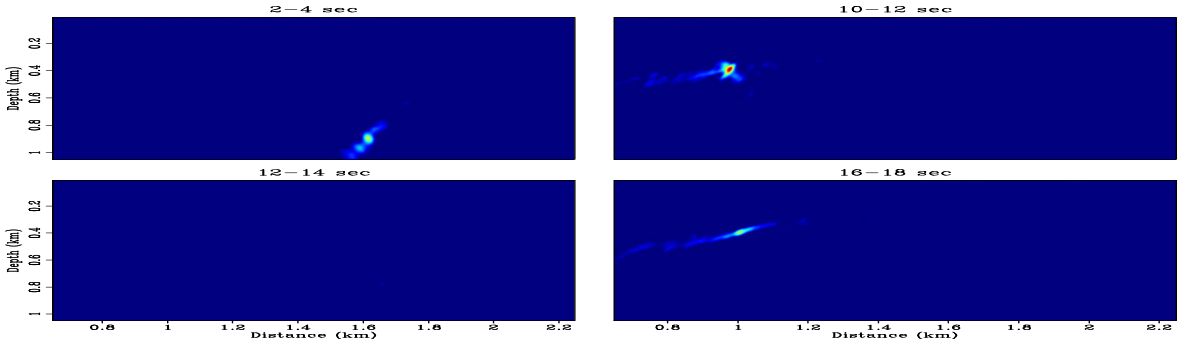

Figure 3 Two second sub-images. Everything below the 99% confidence level of 1.48 is clipped. Only a single all-zero sub-image included.

Picking focii with Lloyd

Methods to quantize or compress functions are numerous in the literature, but all strive to represent a function by the smallest number of meaningful bytes with minimal loss of information. Clapp (2004) introduced the use of Lloyd's Algorithm (LA), or Voronoi iteration, for optimally selecting reference velocities for Fourier-domain wave-equation migrations. The algorithm solves an iterative quantization problem to optimally select a small number of representative values from a large set. We have modified the method to automatically and intelligently find focus locations in images without mandating a minimum (we allow zero) or maximum (can be thousands) number of returned locations.

Because quantization methods are based on selecting representative values of a given function, we must first turn the volume of image amplitudes into a related set of numbers for input to LA: We're interested in the coordinate axes values where high values exist, rather than the distribution of functional amplitude values. Therefore, we build a vector of image coordinate (x,y,z) values that represents the amplitudes within the volume. First the amplitudes are discritized between the minimum confidence threshold and the maximum value. We find that 10 levels are sufficient. Then, locations in space with amplitudes above the threshold are repeatedly entered into the input vector according to the number of quantum levels associated with its amplitude. Locations with amplitude below the confidence threshold, which is most of the domain, are ignored.

Figure 5 shows graphically how the data input into LA is selected from a sampled 1D function. A human will instantly select 2 plausible focii at locations 5.5 and 11.5. Assume that the continuous signal is sampled only at the tick marks on the axis and therefore has 14 amplitude values. The heavy dark line above the axis represents the minimum threshold. The maximum value of the function is at sample 11 or 12. The data values are quantized into three levels. The dots show how many times each coordinate is selected for input. The coordinate set formed from the signal is [4, 5, 5, 6, 6, 10, 11, 11, 11, 12, 12, 12, 13, 13].

The output is a list of optimal locations that best represent the

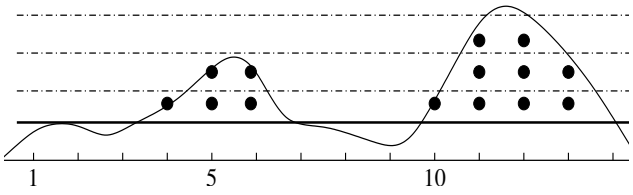

Figure 5 Dots represent coordinate selection by signal amplitude for input into Lloyds Algorithm.

locations of focusing in the image. A tunable parameter is the minimum allowable distance between two selected locations. For the 1D example in Figure 5, LA returns 5 and 12.

Field data

A multi-well pad in a large field development was instrumented with a 414 station grid of single component geophones to monitor subsurface seismicity for approximately 1 month. Miyazawa et al. (2008) present the analysis of microseismicity monitored with a downhole array in a very similar area. The 1D velocity modelfor this pad, derived from several well logs, is that in Figure 2. Figure 6 shows the layout and elevation of the array, the locations of 2 perforation shots, and a fracture event.

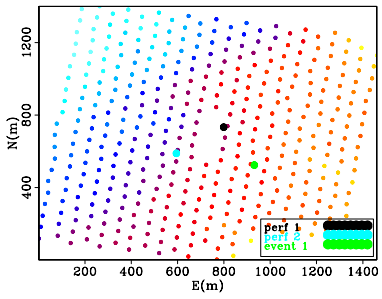

Figure 6 Surface array acquisition and surface projection of all imaging results. Colors are elevation, dipping 60 m from the NW to SE.

Figure 7 is a fracture event after correcting for statics estimated with the perforation shot data. Consistent with modeled data, the multiple hyperbolas after the strongest arrival are intrabed multiples not individual events. Ray based and picking location methods will likely treat these arrivals as separate events.

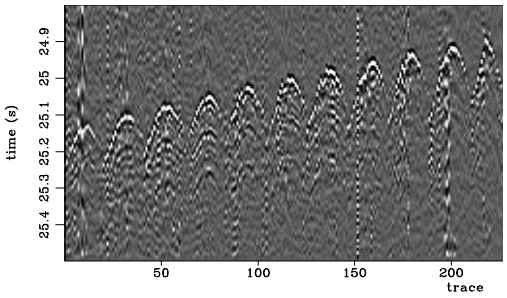

Figure 7 The western 11 lines of event 1 data with bandpass between 10 and 60 Hz. No S-waves are seen on the vertical component data.

Figure 8 is the image of the event in three extractions through the amplitude maximum in the image. The image is zeroed below the 99% confidence threshold. With single component geophones, we were limited to acoustic P-wave imaging. Modelling exercises indicate that for realistic double-couple sources, it is unrealistic to expect S-wave energy to be recorded on the vertical component. The data example supports this. Despite this limitation, there is still radiation pattern information in Figure 8. If one assumes that the failure mechanism results in a double-couple source, one can compare modelled data results with the field data to extract orientation angles that can be related to the stress field.

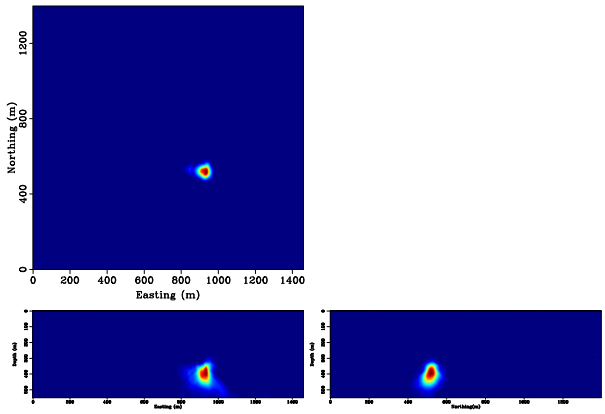

Figure 8 A fracture event image using the data in Figure 7 located at z=396 E=934 N=522.

Conclusions

We present a method to accurately locate microseismic events from long time series data. It requires no manipulation of the data and does not rely on picking arrivals. The error of the location is only a function of the quality of the velocity model. Two propagations the length of the data (the recorded data and the noise model) are required. Short-time sub-images are output for post-processing while the complete time series are propagated through the model domain. Rather than save these many large volumes, we use Lloyd's Algorithm to select meaningful focus locations. The locations, time window in which the event focused, and signal-to-noise ratio are saved to an ascii file. The method is easily adapted to acoustic, elastic, or anisotropic propagators.

TRI volumes show the radiation pattern of events in the image domain. The patterns are indicative to the failure mechanism of the source event, especially for multi-component data. Therefore, discarding all of the volumes results in the loss of valuable information. Individual sub-images using only a few seconds of data are very fast to calculate on GPU-based imaging software. After the large data volume is processed in bulk, interesting events or time windows can be re-processed in a few minutes for further analysis or integration with seismic volumes.

The TRI algorithm is capable of accurately imaging perforation shots and fracture events in the surface array data. Using 1D velocity functions and calculated statics corrections, the perforation shots are within a few meters of the known location. As with all imaging methodologies, the accuracy of the velocity model dictates the accuracy of the TRI result. The algorithmic accuracy, deduced by self-consistent forward-reverse modeling, is approximately one grid cell. Therefore, with a realistic 3D earth model, provided by reflection seismic and well control, field results will converge to the algorithmic accuracy. The use of single component geophones, while not ideal, is sufficient for imaging these events. Acoustic imaging of events is possible, which will be substantially faster then elastic propagation. For large amounts of data this may be the appropriate choice. If the goal is to locate very weak events or characterize non-explosive sources, elastic imaging is required.

Acknowledgements

We appreciate the participation of Zack Lawrence and Anupama Venkataraman from the ExxonMobil Exploration Company, Michael A. Payne of ExxonMobil Upstream Research Company, and Imperial Oil.

REFERENCES

Artman, B., I. Podladtchikov, and B. Witten, 2010, Source location using time-reverse imaging: Geophysical Prospecting, **58**, 861 – 873.

Bardainne, T., E. Gaucher, F. Cerda, and D. Drapeau, 2009, Comparison of picking-based and waveform-based location methods of microseismic events: Application to a fracturing job: SEG Technical Program Expanded Abstracts, **28**, 1547–1551.

Borcea, L., G. Papanicolaou, and C. Tsogka, 2006, Coherent interferometric imaging in clutter: Geophysics, **71**, SI165–SI175.

Chambers, K., O. Barkved, and J.-M. Kendall, 2009, Imaging induced seismicity with the LoFS permanent sensor surface array: SEG Technical Program Expanded Abstracts, **28**, 1612–1616.

Chambers, K., J.-M. Kendall, S. Brandsberg-Dahl, and J. Rueda, 2010, Testing the ability of surface arrays to monitor microseismic activity: Geophysical Prospecting, **58**, 821 – 830.

Clapp, R. G., 2004, Reference velocity selection by a generalized Lloyd method: SEG Technical Program Expanded Abstracts, **23**, 981–984.

Eisner, L., D. Abbott, W. B. Barker, J. Lakings, and M. P. Thornton, 2008, Noise suppression for detection and location of microseismic events using a matched filter: SEG Technical Program Expanded Abstracts, **27**, 1431–1435.

Eisner, L., P. M. Duncan, W. M. Heigl, and W. R. Keller, 2009, Uncertainties in passive seismic monitoring: The Leading Edge, **28**, 648–655.

Maxwell, S. C., J. Rutledge, R. Jones, and M. Fehler, 2010, Petroleum reservoir characterization using downhole microseismic monitoring: Geophysics, **75**, 75A129–75A137.

Miyazawa, M., A. Venkataraman, R. Snieder, and M. A. Payne, 2008, Analysis of microearthquake data at cold lake and its applications to reservoir monitoring: Geophysics, **73**, O15–O21.

Sava, P., 2011, Micro-earthquake monitoring with sparsely sampled data: Journal of Petroleum Exploration and Production Technologies, **10.1007/s13202-011-0005-7**, 1–7.

Schuster, G. T., J. Yu, J. Sheng, and J. Rickett, 2004, Interferometric/daylight seismic imaging: Geophysics Journal International, **157**, 838–852.

Steiner, B., E. H. Saenger, and S. M. Schmallholz, 2008, Time reverse modeling of low-frequency microtremors: Application to hydrocarbon reservoir localization: Geophysical Research Letters, **35**, L03307.

Witten, B., and B. Artman, 2011, Signal-to-noise estimates of time-reverse images: Geophysics, **76**, MA1–MA10.

Xuan, R., and P. Sava, 2010, Probabilistic microearthquake location for reservoir monitoring: Geophysics, **75**, MA9–MA26.